Chapter 21
Far-Field Ocean Conditions and Concentrate Discharges Modeling Along the Saudi Coast of the Red Sea

Peng Zhan, Fengchao Yao, Aditya R. Kartadikaria, Yesubabu Viswanadhapalli, Ganesh Gopalakrishnan and Ibrahim Hoteit

Abstract An integrated modeling system is developed to simulate the far-field dispersions of concentrate discharges along the Saudi coast of the Red Sea. It comprises the Weather Research and Forecast (WRF) model for simulating the atmospheric circulations, the MIT general circulation model (MITgcm) for simulating the large-scale ocean conditions, and the Connectivity Modeling System (CMS) for tracking particle pathways. We use the system outputs and remote sensing altimetry data to study and analyze the atmospheric and oceanic conditions along the Saudi coast of the Red Sea and to conduct particle tracking experiments. The model simulations show distinctive patterns of seasonal variations in both the atmospheric conditions and the large-scale ocean circulation in the Red Sea, which are also reflected in the salinity and temperature distributions along the Saudi coast.

P. Zhan (✉) · F. Yao · A.R. Kartadikaria · Y. Viswanadhapalli · I. Hoteit
Division of Physical Sciences and Engineering, King Abdullah University of Science and Technology, Thuwal, Saudi Arabia
e-mail: peng.zhan@kaust.edu.sa

F. Yao
e-mail: fengchao.yao@kaust.edu.sa

A.R. Kartadikaria
e-mail: aditya.kartadikaria@kaust.edu.sa

Y. Viswanadhapalli
e-mail: y.viswanadhapalli@kaust.edu.sa

I. Hoteit
e-mail: Ibrahim.hoteit@kaust.edu.sa

G. Gopalakrishnan
Scripps Institution of Oceanography, University of California San Diego, San Diego, California
e-mail: ggopalak@ucsd.edu

The impact of this seasonality on the far-field dispersion of concentrate discharges are illustrated in seasonal dispersion scenarios with discharging outfalls located at the northern, central and southern Saudi coasts of the Red Sea.

21.1 Introduction

The Red Sea is a marginal sea located between the Arabian Peninsula and the African continent. This long and narrow basin spans over 2000 km and connects to the Gulf of Aden through the Strait of Bab el Mandeb. The basin bifurcates into the Gulf of Aqaba and the Gulf of Suez at the northern end (Fig. 21.1). The latter connects to the Mediterranean Sea through the Suez Canal with a negligible water exchange (Sofianos et al. 2002).

The Kingdom of Saudi Arabia occupies the largest portion of coast along the Red Sea in the west of the Arabian Peninsula. Not surprisingly, the conditions of the Red Sea profoundly affect people's social and economic lives in the kingdom. In addition, isolated from the world ocean, the Red Sea serves as a sanctuary for a unique marine ecosystem and an ideal habitat for the coral reef community (Berumen et al. 2013). However, the Saudi coast is experiencing large industrial and population expansions including constructions of new cities, massive desalination plants, oil refineries and aquaculture farms. For instance, desalination of seawater, serving as a reliable and drought-proof source of local water supply, is becoming increasingly important for the Kingdom. The released brine and chemical discharges should be effectively diluted and transported into the far-field sea, otherwise, effluent discharges of wastewater or brines would adversely affect the local marine ecosystem and aquatic resources in the inshore coastal areas. It is, therefore, crucial to study and evaluate the environmental influence of such human activities on the Red Sea in order to mitigate their impacts and to optimally utilize the coastal resources.

As in any other sea, dispersion of outfall concentrate discharges in the Red Sea is controlled by two different dynamical stages. In the first stage near the outfall, the concentrate usually possesses highly negative buoyancy compared with the ambient seawater and, as a result, undergoes significant mixing and diluting. In the second stage, when the concentrate reaches a neutral buoyancy condition with the ambient seawater, the dispersion is primarily controlled by the advection and diffusion of the large-scale circulation in the Red Sea. While the dynamical modeling of the first stage calls for near-field non-hydrostatic hydrodynamic models with fine resolutions in both horizontal (in the order of tens of meters) and vertical (in the order of meters) directions, the far-field modeling of the dispersion occurring in the second stage often involves hydrostatic ocean general circulation models with relatively lower resolution (few kilometers). Because the initial dilution in the first stage also depends on the vertical stratification and currents in the ambient seawater, the large-scale circulation in the Red Sea is important for both the near-field and far-field modeling.

Fig. 21.1 Map of the Red
Sea topography and model
domain for the Red Sea
MITgcm
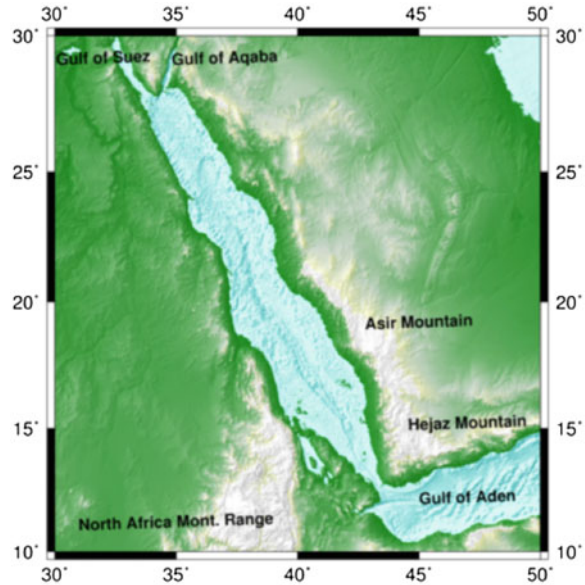
The large-scale ocean circulation in the Red Sea is a coupled response to the
atmospheric forcing and the water exchanges with the Indian Ocean through the
Strait of Bab el Mandeb (Sofianos and Johns 2002). The atmospheric forcing
includes surface heat flux, excessive freshwater loss due to evaporation, and wind
stress. All the components of the atmospheric forcing show strong seasonal varia-
tions, driving a seasonally reversing overturning circulation in the Red Sea (Yao et al.
2014b). During winter, cold and high-salinity water is formed in the northern Red Sea
due to heat loss and evaporation and is exported to the Gulf of Aden as a deep
outflow, compensated by a surface inflow from the Gulf of Aden (Yao et al. 2014a).
In response to the reversal of the surface winds in the Red Sea and the Arabian Sea
during the summer Indian monsoon, the summer overturning circulation is strikingly
reversed from the winter overturning circulation, and is composed of a surface
outflow, a subsurface intrusion from the Gulf of Aden and a greatly reduced deep
outflow. Despite the narrowness of the basin, the circulation in the Red Sea also
exhibits strong lateral variability associated with boundary currents and meso-scale
eddies throughout the year as suggested by modeling studies and satellite sea level
anomaly data (Yao et al. 2014b; Zhai and Bower 2013; Zhan et al. 2014).

In this chapter, we first analyze remote sensing altimetry data to examine the
large-scale background flow and the seasonal variation of sea level in the Red Sea.
This would provide the basic information about the general circulation occurring in
this region. We then present the development of an integrated modeling system to
simulate the atmospheric conditions, the general ocean circulation, and particle
dispersion, based on the atmospheric and oceanic conditions as well as their
seasonalities over the Red Sea region, especially along the Saudi coast, are

described and analyzed. Using these model outputs, we conduct particles releasing experiments to illustrate the far-field dispersion of concentrate discharges under different seasonal scenarios along the Saudi coast of the Red Sea.

The remaining part of the chapter is organized as follows. Section 21.2 analyzes the sea level anomalies and absolute dynamic topography remote sensing data. Section 21.3 introduces the integrated modeling system. The simulated atmospheric and oceanic conditions are described in Sect. 21.4. Section 21.5 presents the results of far-field concentrate discharges experiments released along the Saudi coast. Section 21.6 concludes with a summary and a discussion of future work.

## 21.2 Sea Level Variations

The currents in the meso- and large-scale ocean circulation are reflected by the sea level through the geostrophic relationship. In this section, we analyze the Archiving Validation and Interpretation of Satellite Data in Oceanography (AVISO) altimetry and discuss the seasonal variations of sea level in the Red Sea, focusing on the Saudi coast.

Sea level anomalies (SLA) represent the variations of the sea surface height relative to the mean sea surface (MSS). We use the AVISO merged product of TOPEX/POSEIDON, Jason-1, Envisat and European Research Satellite (ERS) (Dibarboure et al. 2008), computed with the MSS CNES-CLS-2011 referenced to a 20-year period from 1993 to 2012, available at ftp://ftp.aviso.altimetry.fr/global/delayed-time/grids/. AVISO also provides the absolute dynamic topography (ADT), from which the mean dynamic topography (MDT) which can be obtained as MDT = ADT − SLA. Serving as the reference surface to ADT, the MDT represents the sea level variation associated with the stationary components (long-term mean currents) of ocean dynamics. Our analyses are based on monthly data with a resolution of $1/4°$ from January 1993 to December 2012.

In the Red Sea, the MDT increases northward from the Strait of Bab el Mandeb up to $\sim 18°N$, before gradually decreasing all the way to the north as shown in Figs. 21.2 and 21.3. The sea level bulge in the central Red Sea was attributed to the surface winds pattern by Sofianos and Johns (2001). The different slope of MDT between the southern and northern Red Sea indicates opposite geostrophic currents flowing westward south of $\sim 18°N$ and eastward in the central and northern Red Sea. In the central basin between $\sim 18°N$ and $\sim 24°N$, where the slope is relatively steep, the flow exhibits a larger geostrophic velocity, up to 0.2 m/s. This mean stationary eastward geostrophic current in the northern and central Red Sea transports considerable water eastward across the basin to the Saudi coast.

Superimposed on the background flow, eddies and boundary currents also play a key role in transporting kinetic energy, heat, and biogeochemical particles within the basin of the Red Sea. These time-varying dynamics are generally more energetic than the background flow and they may even dominate the structure of the circulation. Information about their features cannot be derived from MDT, but from SLA.

**Fig. 21.2** The MDT and the associated geostrophic current
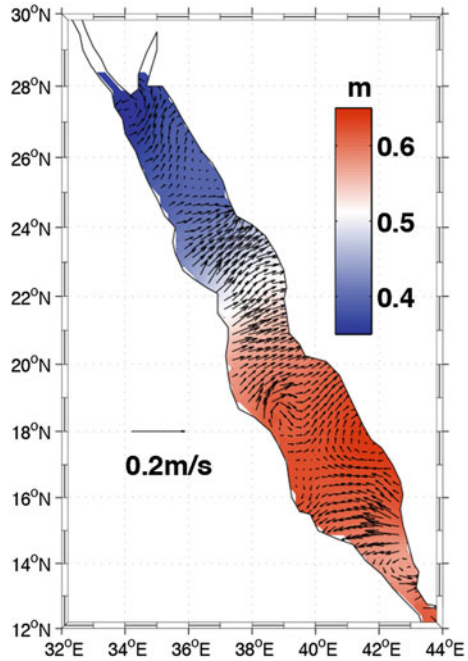
Fig. 21.3 The scatter plot of MDT as a function of latitude (*black cross*) and its zonal mean (*red solid curve*)
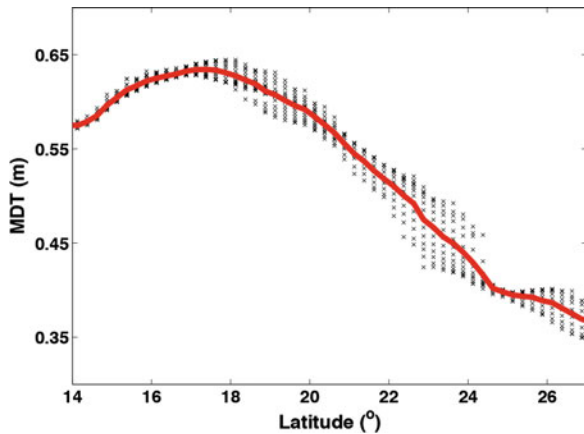
To study both the temporal and the spatial patterns of the SLA in the Red Sea, the 20-year monthly mean AVISO SLA data are analyzed using an Empirical Orthogonal Functions (EOF) analysis. The EOF analysis extracts the dominant modes from a spatio-temporal dataset according to their overall variance contributions (Emery and Thomson 2001). The EOF modes can be used to analyze the spatial variability of SLA, while the time series of their principal components (PCs) quantify their evolution over time.

The EOF analysis of SLA in the Red Sea shows that the first mode accounts for 89 % of the total variance, indicating the absolute dominance of the leading mode. As shown Fig. 21.4a, the first EOF mode of the monthly SLA is positive throughout the entire Red Sea basin. The uniform sign suggests that the SLA would rise and fall in phase over the entire basin of the Red Sea, with remarkable eddy variability in the central and northern Red Sea. Figure 21.4b suggests that the climatological mean PC time series of the first EOF mode exhibits a prominent seasonal cycle, with a peak in January and a trough in August. The sign shifts that occur in May-June (from positive to negative) and in October–November (from negative to positive) mark the shift of anomaly relative to the MDT. Given that the first EOF mode is positive across the basin, the SLA is predominantly higher/lower than the MDT during winter/summer over the entire Red Sea. Larger variability of SLA is observed along the Saudi coast than along the African coast, with the largest annual variation of ∼0.4 m appearing in the central basin at about 19°N. This seasonal reversal of the tilting of SLA implies that the associated geostrophic current is generally northward during winter and southward during summer.

The variations of SLA in the Red Sea can be largely attributed to the seasonal differences in the atmosphere. The Red Sea basin is indeed separated into two parts according to the wind seasonal regimes (Jiang et al. 2009). In the northern part of the basin the wind blows from the northwest all around the year. However, the northeast Indian Monsoon controls the surface wind distinctively over the basin south of ∼19°N, reversing from northwesterly during summer (June–October) to southeasterly during winter (November–May). The variation of SLA in the southern
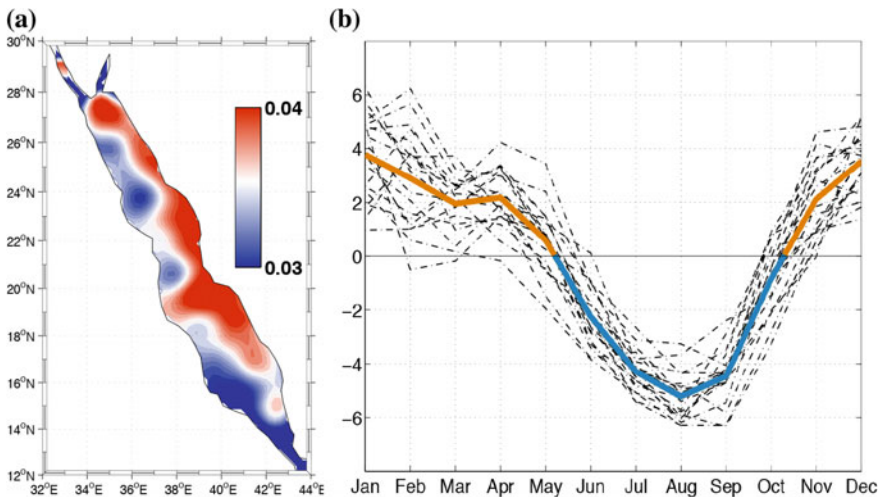
Fig. 21.4 a The first EOF mode of the monthly SLA. **b** Monthly standard deviations of the PC time series associated with first EOF mode. The *black dot curves* represent the time series in each year from 1993 to 2012, and the *solid colored curve* represents the climatological mean during that period, where the *yellow*, *blue parts* show the positive, negative period, respectively

Red Sea could partly be explained by the Ekman transport associated with the seasonally reversing winds. The southeasterly winds during winter (northwesterly during summer) transports water to the east (west) and cause a higher SLA along the Saudi (African) coast. The alternation of wind patterns over the southern basin agrees remarkably well with the first PC of SLA. Similarly, in the northern Red Sea, the northwesterly winds during summer leads to a western transport causing a higher SLA along the African coast. Nevertheless, the higher SLA along the Saudi coast during winter cannot be easily explained as it contradicts with the westward Ekman transport associated with the northwesterly winds. One can therefore expect a northward compensation boundary current along the Saudi coast during winter, which is reported by Yao et al. (2014a) from a model point of view.

21.3 Modeling System

This section describes the integrated modeling system that has been developed to simulate the atmospheric and oceanic conditions, and the resulting concentrate discharges in the Red Sea. The system consists of the Weather Research and Forecasting (WRF) model (Michalakes et al. 2005), the regional nested MIT general circulation model (MITgcm) (Marshall et al. 1997a, b), and the Connectivity Modeling System (CMS) (Paris et al. 2013).

21.3.1 Atmospheric Model—WRF

The atmospheric conditions are simulated using the Advanced Research WRF (ARW) (Skamarock et al. 2008). The model is configured over the Red Sea and is nested within a larger domain covering the central Middle East and North Africa. The horizontal resolution is 30 km for the coarse resolution model and 10 km for the finer resolution model, both configured with 35 vertical levels. Initial and boundary conditions for WRF are obtained from the National Center for Environmental Prediction (NCEP) Final Analysis (FNL) product. Observations available from the Atmospheric Data Project (ADP) are assimilated into WRF using a 3-Dimensional Variational (3DVAR) data assimilation technique. An atmospheric reanalysis product is generated for the Red Sea using this assimilative WRF by daily initializing the model at 12 UTC using the consecutive integration method (Langodan et al. 2014; Lo et al. 2008). The ADP observations are assimilated every 6-h for a period of 36 h using the respective WRF forecast as background in the next assimilation cycle. The first 12-h simulation serves as the model spinning-up period, and is thus neglected. For better representation of land-sea contrast in WRF over coastal regions, we modified the lower boundary conditions by replacing the

coarse-resolution SST from FNL with high-resolution SST from the Real-Time Global High-Resolution (RTG-HR). The model physics adopted in WRF are the same as those in Jiang et al. (2009).

21.3.2 Ocean Model—MITgcm

The large-scale circulation in the Red Sea is simulated using the MITgcm. The MITgcm is a primitive-equation oceanic general circulation model solving the Navier-Stokes equations under the Boussinesq approximation. The model equations are discretized in z coordinates in the vertical direction and, for each level, are configured in a staggered Arakawa C-grid. The MITgcm includes both non-hydrostatic and hydrostatic formulations. It is implemented here in hydrostatic mode with an implicit free surface. The model domain extends from 10°N to 30°N and from 30°E to 50°E (Fig. 21.1), covering the entire Red Sea basin, the Gulf of Aqaba and the Gulf of Suez in the north end, as well as the Gulf of Aden, where the only (eastern) open boundary is located. The model has a horizontal resolution of 4 km and 50 vertical layers with thicknesses ranging between 4 m at the sea surface up to 300 m at the sea bottom. The model topography is generated from the General Bathymetric Chart of the Ocean (Ioc 2003). The model is integrated from January 2000 to December 2010, forced with the 3-hourly Red Sea WRF atmospheric fields, including momentum, heat and fresh water fluxes. The eastern boundary is nested within a large-domain coarser MITgcm configured for the Arabian Peninsula including the Arabian Sea. The results between 2009 and 2010 are presented in this study.

21.3.3 Connectivity Model—CMS

Forward simulation of passive particles is widely used to estimate a range of likely water concentrate discharges in the ocean (Haza et al. 2007; Piterbarg 2001; Veneziani et al. 2004, 2005). This is a challenging problem for the Red Sea because of the seasonally varying wind and current conditions. In this study, the trajectories of individual-based particles from pre-specified point source regions are simulated using the CMS. CMS is a multi-scale probabilistic model of particle dispersal based on a stochastic Lagrangian framework. The Lagrangian formulation for particle dispersion is a powerful tool to study and analyze the hydrodynamic behavior of fluids (Hegarty et al. 2013; Stohl et al. 2005). Given a velocity field, often resulting from a general circulation model, the CMS calculates particle locations and keeps track of their pathways following a multiple and multi-grid approach.

  CMS can be used to simulate phenomena such as advection, dispersion and retention. It could be configured to distinguish the particles that either settle on the topography or swim away, and therefore may be beneficial for a broad range of

applications, ranging from the dispersion of contaminant plumes from discharges and deep-water ventilation, to larval migrations and probability of population connectivity. In this study, the trajectories of passive particles are calculated with CMS based on daily averaged 3-Dimensional velocity fields as simulated by the Red Sea MITgcm.

21.4 Simulated Atmospheric and Oceanic Conditions

This section first describes the key features of the atmospheric conditions along the Saudi coast based on the WRF simulation results. This is followed by an analysis of the large-scale ocean circulation and hydrographic properties in different seasons in the Red Sea as simulated by the MITgcm.

21.4.1 Atmospheric Conditions

To describe the seasonal variability of the general atmospheric conditions over the Red Sea, especially along the Saudi coast, Hovmoller diagrams of the surface winds and surface air temperature are plotted based on the WRF outputs.

As shown in Fig. 21.5, the wind field over the Saudi coast exhibits considerable seasonality. In summer (from June to October), northwesterly winds originated from the Mediterranean region persist along the Saudi coast. In winter (from November to April), the region north of ∼20°N is dominated by northwesterly winds, forming a convergence zone at about 19°N with the topographically diverted southeasterly winds blowing from through the Gulf of Aden. These converging winds funnel out through the Tokar gap. It is reported that the strength of the wind
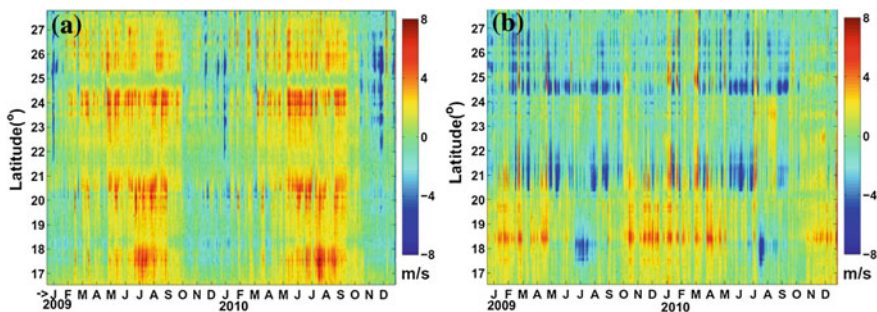
Fig. 21.5 **a** The Hovmoller diagram of the zonal surface winds along the Saudi coast of the Red Sea. **b** The hovmoller diagram of the meridional surface winds along the Saudi coast of the Red Sea

Fig. 21.6 The Hovmoller
diagram of the surface air
temperature along the Saudi
coast of the Red Sea
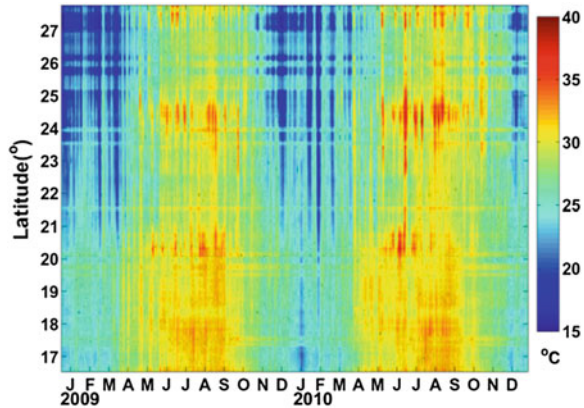
and its direction depends on the seasonal movement of the Inter Tropical Convergence Zone (ITCZ) (Jiang et al. 2009).

The orography has a profound influence on the local dominant wind regimes (Jiang et al. 2009; Ralston et al. 2013). The Red Sea is indeed surrounded by high mountain ranges that constrain the winds to blow along the axis of the basin, except for some gaps where valleys cutting across the mountain ridges generate unique local wind flows. Intense across-basin winds (Fig. 21.5) are associated with mountain gaps located at latitudes 23.5–24.5°N, 20–21°N and 17–18°N. These wind jets could reach up to 15 m/s, and transport a large amount of dust towards the Arabian Peninsula during summer and bring moist subtropical air towards the Southern Sudan region during winter.

Figure 21.6 shows that the surface air temperature also exhibits an obvious seasonal cycle along the Saudi coastline of the Red Sea. The air temperature between November and April exhibits cooler patterns than the summer months throughout the whole coastline, with generally a northward decreasing trend. Apart for the latitudinal variation of heat flux, the tropical monsoonal air transported by the southeasterly winds could be also responsible for the warm features along the southern Saudi coast during the winter. The temperature in summer exhibits multiple peaks (≥36 °C) at 17–18°N, 20–21°N, and 24–25°N. These locations correspond remarkably well with the mountain gaps, through which across-basin African and Arabian hot wind jets blow. Overall, Figs. 21.5 and 21. 6 reveal that local wind circulation has a significant influence on the surface temperature distribution.

21.4.2 General Circulation in the Red Sea

Overall, the large-scale circulation and vertical structure in the Red Sea manifest a complex pattern that varies seasonally, latitudinally and longitudinally. This subsection describes the typical winter and summer surface circulations along three
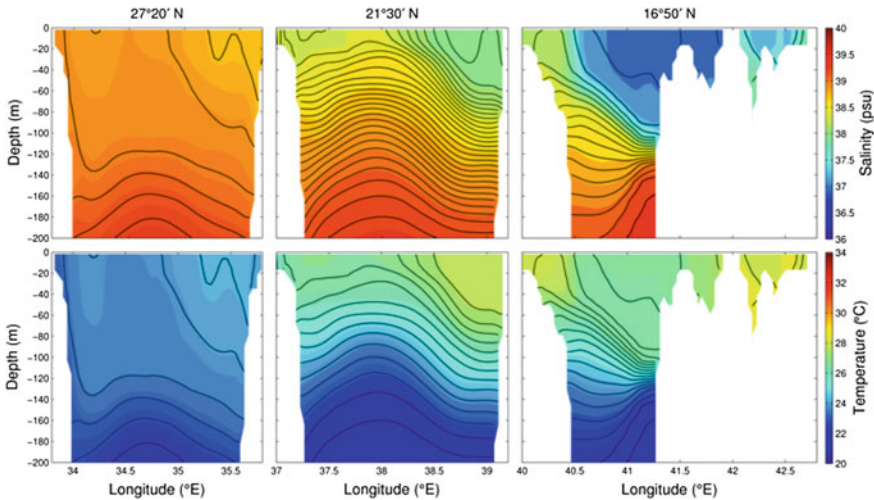
zonal sections located in the northern, central and southern Red Sea as simulated by the MITgcm. This provides relevant information for the far-field modeling of concentrate discharges along the Saudi coast.

The winter surface circulation for February 2009 is displayed in Figs. 21.7a, b, and the vertical sections at latitudes 27° 20′N, 21° 30′N, and 16° 50′N are depicted in Fig. 21.8. As the upper branch of the overturning circulation, the winter surface current field in the Red Sea is characterized by an intruding low-salinity inflow from the Gulf of Aden. The inflow initially appears as a western boundary current but is unidentifiable north of 20°N, where a chain of alternating meso-scale eddies dominate. Saline (∼40 psu) and cold (∼22 °C) water is found in the northern basin, where the sinking in the winter overturning circulation occurs as shown in the climatological results in Yao et al. (2014b). As the surface density gradually increases towards the north, the vertical structures across the basin show a general trend of decrease in stratification, with an almost uniform vertical structure in salinity and temperature appearing in the northern section. In each vertical section, the stratification around the Saudi coast is weak as suggested by the almost vertical isopycnals, but the stratification becomes more evident along the African coast, particularly in the southern Red Sea, where the isopycnals tilt upward to the west.

As the surface heat flux changes from cooling to warming and the summer Indian monsoon is established in the region, the surface circulation and vertical structure in the Red Sea from June to September differ drastically from the winter
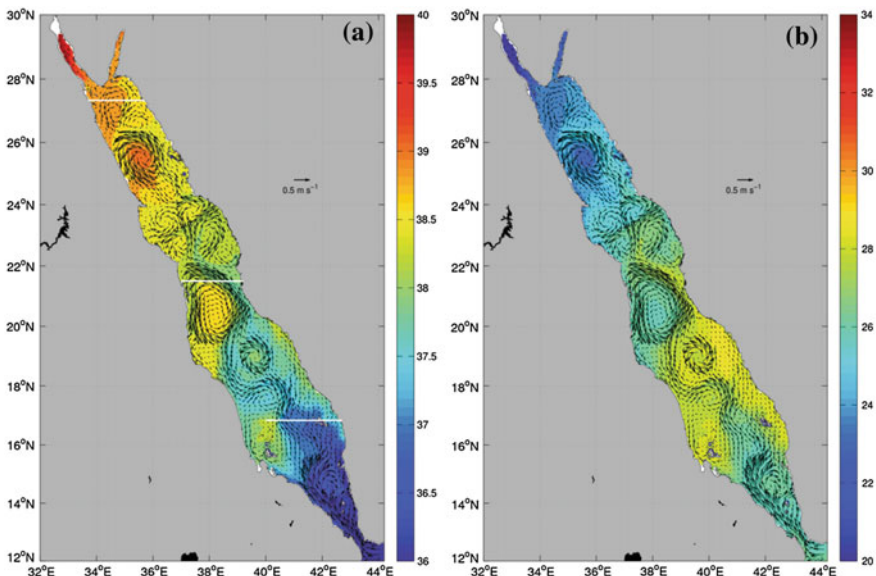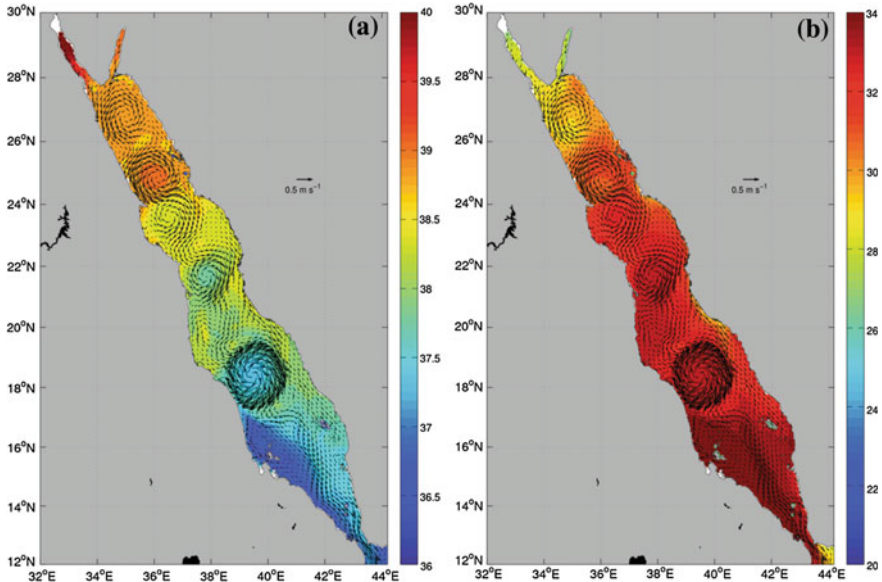

Fig. 21.7 **a** Surface current and salinity fields for the February 2009 MITgcm model results. The *white lines* denote the locations of the vertical sections across the basin. **b** Surface current and temperature fields for the February 2009 MITgcm model results

Fig. 21.8 Vertical sections of salinity and temperature in the northern, central and southern Red Sea for the February 2009 MITgcm results. Also plotted are the contours of potential density with a interval of 0.2 kg m^{-3}. The contour intervals of the locations of each section are donated in Fig. 21.7a

condition (Figs. 21.9a, b and 21.10). The surface currents in the Red Sea reverse to a southward outflow that increases the surface salinity in the southern basin. The surface water is greatly warmed up in the entire basin, with a maximum temperature of about 34 °C. The meso-scale eddies in the Red Sea appear more organized than in winter, and a strong anti-cyclonic eddy emerges around 18°N as a result of the Tokar Jet blowing from the African coast (Zhai and Bower 2013). In contrast to the winter season, the surface heating during summer re-establishes or enhances the vertical stratification in the Red Sea, and the isopyncals at the central and southern section tend to tilt upward to the east. This structure is associated with coastal upwelling driven by the northwesterly surface winds during summer (Fig. 21.9). In the southern section, the subsurface intrusion is manifested as fresh and cold water along the Saudi coast at a depth of about 100 m.

Complete seasonal cycles of the surface hydrographic properties along the Saudi coast are shown in Fig. 21.11. The seasonal cycle of the surface salinity closely corresponds to the seasonal reversal of the surface circulation. From October to May, the surface salinity along the Saudi coast is gradually freshened by the surface inflow with the salinity front retreating to the north. From June to September, the high-salinity water in the north is advected towards the south, causing a substantial salinity increase along the Saudi coast. In contrast, the seasonal pattern of the surface temperature is more of a response to the seasonal heat flux over the surface of the Red Sea, and two contrasting seasonal regimes can be recognized, with the coldest surface temperature reached in February in the northern end and the warmest in September between 14 and 18°N.

Fig. 21.9 a Surface current and salinity fields for the August 2009 MITgcm model results. **b** Surface current and temperature fields for the August 2009 MITgcm model results
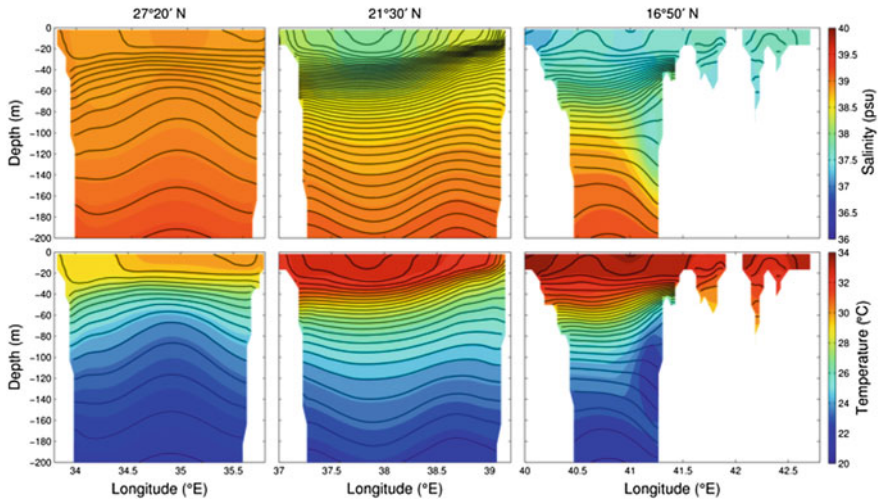
**Fig. 21.10** Same as in Fig. 21.8, except for the results in August 2009
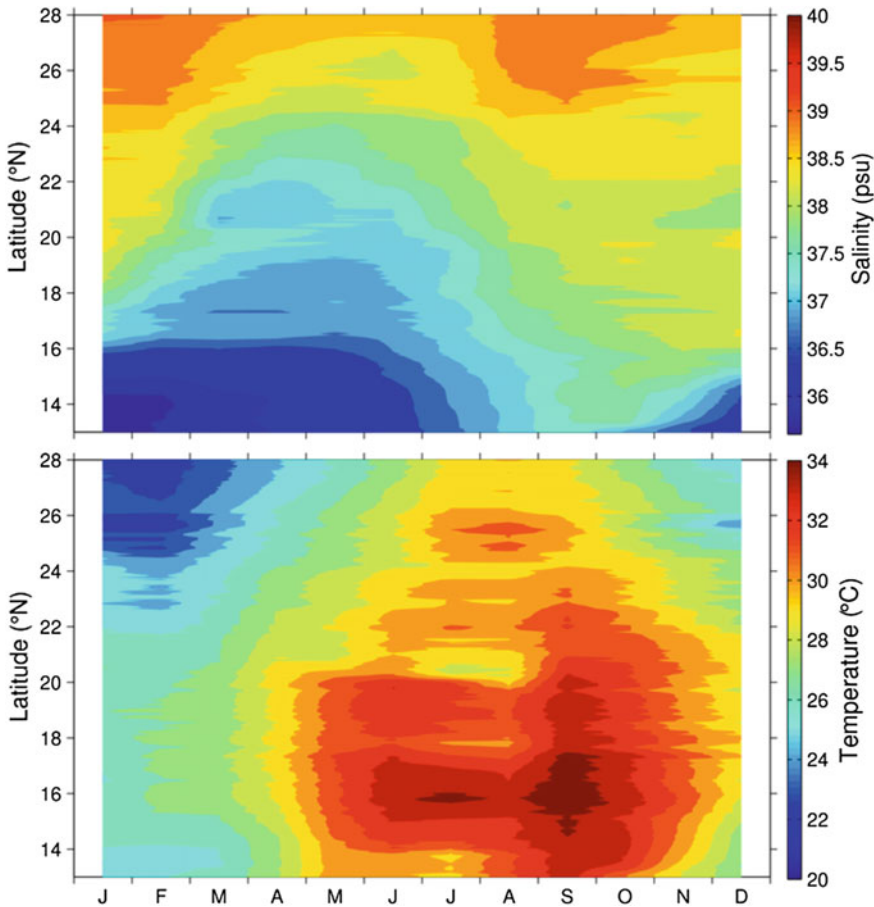
Fig. 21.11 Seasonal cycles of salinity (*top*) and temperature (*bottom*) distributions along the Saudi coast in the 2009 MITgcm results

21.5 Dispersion Experiments and Results

To evaluate the water concentrate discharges situation in the far-field under the Red Sea seasonal conditions, the CMS is implemented based on the 3-dimensional velocity fields obtained from the 4-km Red Sea MITgcm, and the results from 2009 to 2010 are presented. The particles are released as ensembles from polygons offshore of three main Saudi industrial cities along the Red Sea coast: Duba (27.3439°N, 35.6931°E), Jeddah (21.3231°N, 39.0985°E) and Jizan (16.8625°N, 42.5463°E), on June 5th 2009 for the summer scenario and on December 5th 2009 for the winter scenario. Each simulation was run offline for 150 days with daily averaged outputs from MITgcm.

As can be seen from Figs. 21.12 and 21.13, the particles released offshore of Duba in summer are trapped by a cyclonic eddy that flows counterclockwise in the northern end of the Red Sea. It takes about one month for the particles to move from Duba to the western side. The particle trajectories exhibit weak dispersion during the first two months after being released then gradually expand while sinking down from the African coast to the interior of the northern basin. In winter, the particles released offshore of Duba are transported counterclockwise along the northern coast. Some particles enter the Gulf of Aqaba and the Gulf of Suez, but the majorities are transported to the west and move southward along the African coast with rapid sinking reaching depths over 200 m or more. This area was also reported as the region where the major water sinking in the Red Sea overturning circulation occurs (Yao et al. 2014b).

Figure 21.14 suggests that some particles released offshore of Jeddah in summer meander towards the northern end of the basin where they sink down into depths over 120 m. Other particles are trapped into an eddy in the central basin and circulate locally while sinking to the deep layers. These results suggest the possibility of substantial long-distance advection for the particles released in the summer from Jeddah. According to Fig. 21.15, the particles released offshore of Jeddah in winter remain in the shallow water and flow northward following a narrow pathway until ~26°N, where they get trapped in a complex eddy system that amplifies the diffusion of particles. This reinforces mounting evidences that eddies play a crucial role in transporting concentrate discharges in the Red Sea.
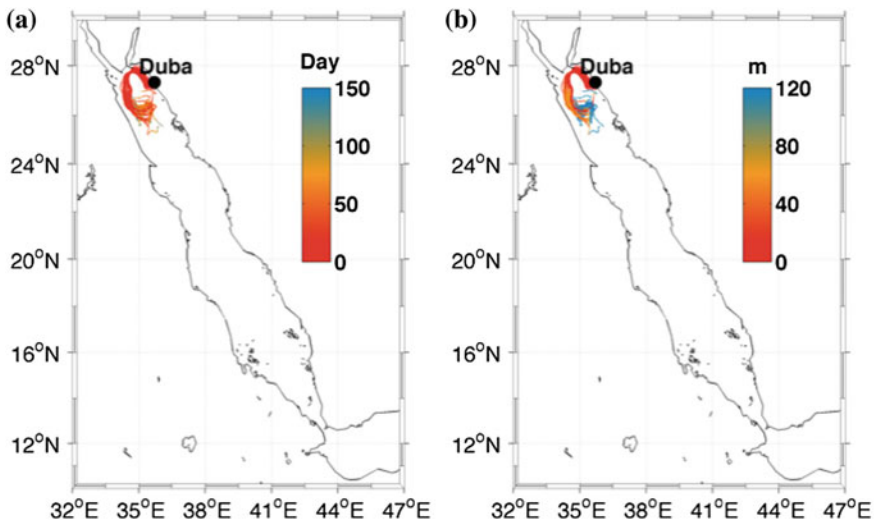
Fig. 21.12 The trajectories of particles released offshore of Duba on June 5th 2009. The *black dot* shows the releasing location and the lines depict particle trajectories with color representing **a** number of days after releasing and **b** depth, respectively
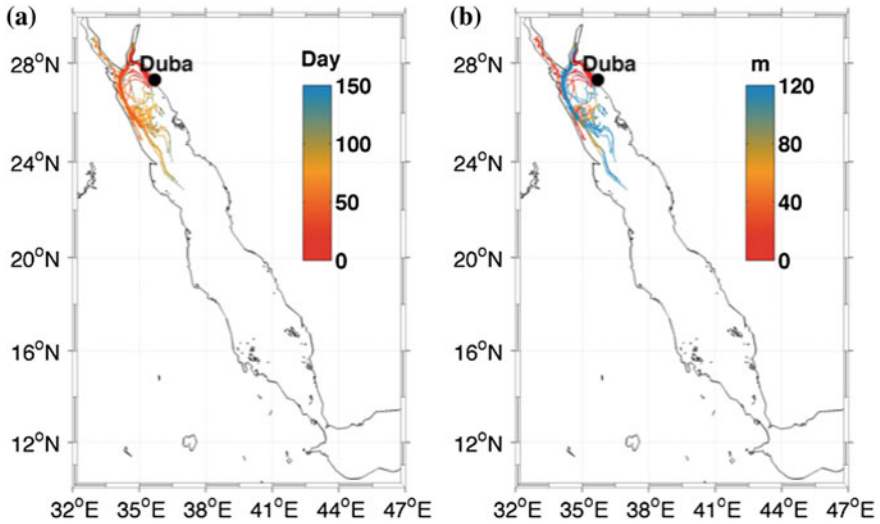
Fig. 21.13 Same as in Fig. 21.12, except for the trajectories of particles released offshore of Duba on December 5th 2009
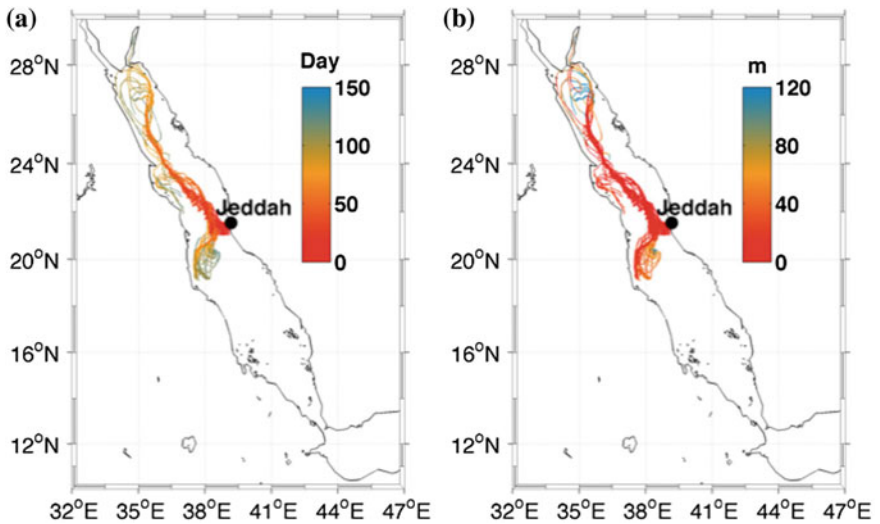

Fig. 21.14 Same as in Fig. 21.12, except for the trajectories of particles released offshore of Jeddah on June 5th 2009

The particles released in the Red Sea may even affect regions outside the basin. As can be seen from Fig. 21.16, the particles released offshore of Jizan in summer remain clustered and flow with the southward current along the Yemeni coast. After they reach the Gulf of Aden, some of the particles flow eastwardly along the
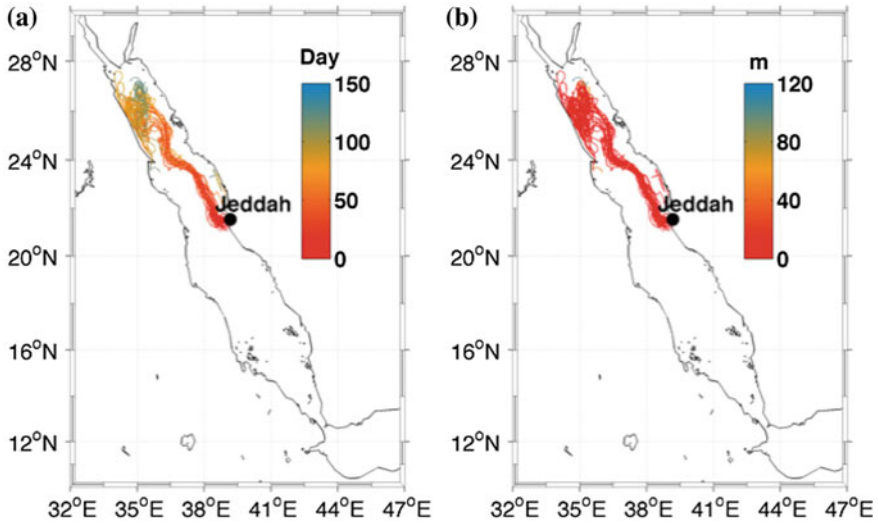
Fig. 21.15 Same as in Fig. 21.12, except for the trajectories of particles released offshore of Jeddah on December 5th 2009
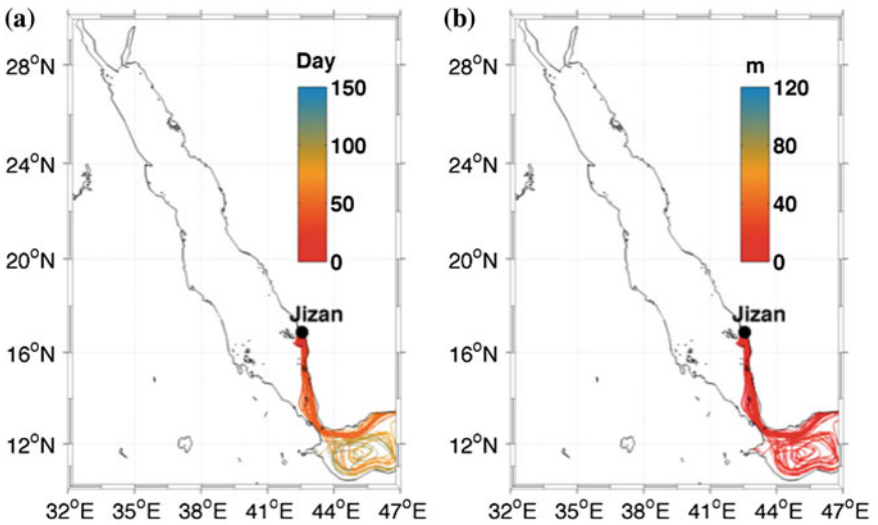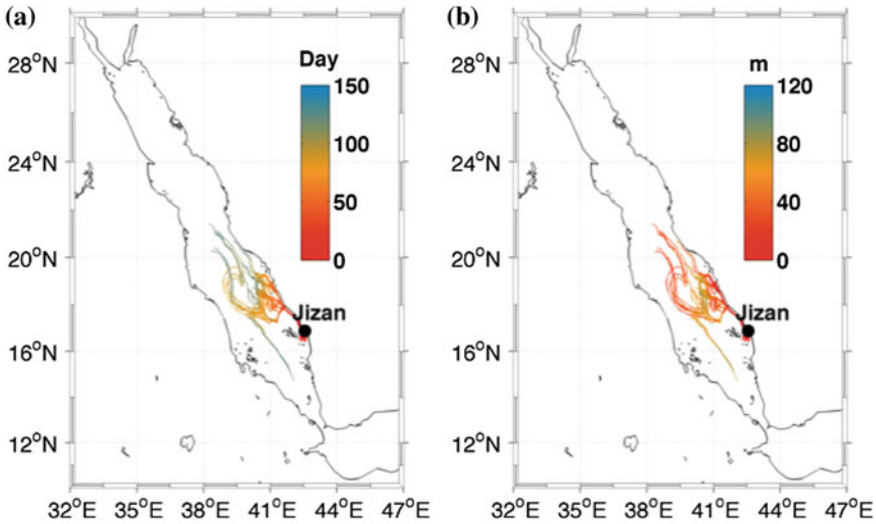

Fig. 21.16 Same as in Fig. 21.12, except for the trajectories of particles released offshore of Jizan on June 5th 2009

southern Yemeni coast, and others are trapped in a cyclonic eddy located right outside the Strait of Bab el Mandeb. No obvious sinking is occurring for these particles. In contrast, the particles released offshore of Jizan in winter (Fig. 21.17) move northward along the Saudi coast before they get trapped by an eddy located at

Fig. 21.17 Same as in Fig. 21.12, except for the trajectories of particles released offshore of Jizan on December 5th 2009

$\sim 18°N$, where a small portion sinks down to a depth of about 50 m and then are advected to the south. The remaining particles in the upper layers meander towards the north, and then gradually spread over the central basin.

21.6 Summary and Discussion

This chapter examined the dispersion of concentrate discharges along the Saudi coast under the complex seasonal atmospheric and oceanic conditions in the Red Sea. The analysis of remote sensing altimetry data revealed a dominant eastward stationary background flow in the Red Sea basin. The sea level exhibits a significant seasonal cycle, with the Saudi coast subject to a larger sea level variation than the African coast. In addition to the observations, we have presented an integrated modeling system for the Red Sea to study the atmospheric and oceanic circulations, focusing on the Saudi coast, and to simulate particles discharges under different seasonal scenarios. The general near-surface winds over the Red Sea are oro-graphically steered to flow along the main axis of the basin due to the high mountain ranges surrounding the basin, with significant seasonal variations. The seasonal variations of atmospheric forcing and water exchanges with the Gulf of Aden determine the seasonal hydrodynamics features of the Red Sea, including pronounced eddy variability, stratification distribution, and overturning circulation. The patterns of the particle trajectories significantly vary with seasons due to the reversal of the seasonal circulation. The far-field simulations of particle trajectories

suggest that boundary currents and eddies play a crucial role in spreading the concentrate discharges from the Saudi coastal regions into the open sea. Our results suggest that eddies and boundary currents may have a great influence on transporting kinetic energy, heat, and biogeochemical particles in this long and narrow basin. Moreover, the distinct seasonal overturning circulation may also affect the coastal mixing and marine productivity. These important factors will be investigated in future studies.

An extension of this modeling system is to couple both near-field and far-field simulations. To achieve the near-field first-stage simulation, the modeling system needs to be configured with the non-hydrostatic mode and much finer resolution to accurately evaluate the dispersal distances of particulate and concentrate discharges, and to provide a framework for evaluating what aspects of the circulations influence the most the distribution and transport of the particles. Aside from tracking the particles trajectories, monitoring the evolution of tracers and concentrations distributions is also of great importance. We will extend the capabilities of our modeling system to simulate and investigate more aspects of potential discharges impacts on the coastal ecosystem of the Red Sea.

References

Berumen, M. L., et al. (2013). The status of coral reef ecology research in the Red Sea. *Coral Reefs, 32*(3), 737–748. doi:10.1007/S00338-013-1055-8.

Dibarboure, G., Lauret, O., Mertz, F., Rosmorduc, V., & Maheu, C. (2008). SSALTO/DUACS user handbook:(M) SLA and (M) ADT near-real time and delayed time products. *Rep. CLS-DOS-NT, 6*, 39.

Emery, W. J., & Thomson, R. E. (2001). *Data analysis methods in physical oceanography* (2nd ed.). Amsterdam: Elsevier.

Haza, A. C., Piterbarg, L. I., Martin, P., Ozgokmen, T. M., & Griffa, A. (2007). A Lagrangian subgridscale model for particle transport improvement and application in the Adriatic Sea using the Navy Coastal Ocean Model. *Ocean Modelling, 17*(1), 68–91. doi:10.1016/J.Ocemod.2006.10.004.

Hegarty, J., Draxler, R. R., Stein, A. F., Brioude, J., Mountain, M., Eluszkiewicz, J., et al. (2013). Evaluation of Lagrangian particle dispersion models with measurements from controlled tracer releases. *Journal of Applied Meteorology and Climatology, 52*(12), 2623–2637. doi:10.1175/Jamc-D-13-0125.1.

Ioc, I. (2003). *BODC, 2003. Centenary edition of the GEBCO Digital Atlas, published on CD-ROM on behalf of the Intergovernmental Oceanographic Commission and the International Hydrographic Organization as part of the general bathymetric chart of the oceans*. Liverpool, United Kingdom: British Oceanographic Data Centre.

Jiang, H., Farrar, J. T., Beardsley, R. C., Chen, R., & Chen, C. (2009). Zonal surface wind jets across the Red Sea due to mountain gap forcing along both sides of the Red Sea. *Geophysical Research Letters, 36*(19), L19605. doi:10.1029/2009GL040008.

Langodan, S., Cavaleri, L., Viswanadhapalli, Y., & Hoteit, I. (2014). The Red Sea: A natural laboratory for wind and wave modeling. *Journal of Physical Oceanography*. Accepted with ref no: JPO-D-13-0242.

Lo, J. C. F., Yang, Z. L., & Pielke, R. A. (2008). Assessment of three dynamical climate downscaling methods using the weather research and forecasting (WRF) model. *Journal of Geophysical Research*: *Atmospheres*, *113*(D9).

Marshall, J., Adcroft, A., Hill, C., Perelman, L., & Heisey, C. (1997a). A finite-volume, incompressible Navier Stokes model for studies of the ocean on parallel computers. *Journal of Geophysical Research: Oceans, 102*(C3), 5753–5766. doi:10.1029/96jc02775.

Marshall, J., Hill, C., Perelman, L., & Adcroft, A. (1997b). Hydrostatic, quasi-hydrostatic, and nonhydrostatic ocean modeling. *Journal of Geophysical Research: Oceans, 102*(C3), 5733–5752. doi:10.1029/96jc02776.

Michalakes, J., Dudhia, J., Gill, D., Henderson, T., Klemp, J., Skamarock, W., et al. (2005). The weather research and forecast model: Software architecture and performance. *Use of High Performance Computing in Meteorology*. 156–168, doi:10.1142/9789812701831_0012.

Paris, C. B., Helgers, J., Van Sebille, E., & Srinivasan, A. (2013). Connectivity modeling system: A probabilistic modeling tool for the multi-scale tracking of biotic and abiotic variability in the ocean. *Environmental Modelling and Software, 42*, 47–54.

Piterbarg, L. I. (2001). Short-term prediction of Lagrangian trajectories. *Journal of Atmospheric and Oceanic Technology, 18*(8), 1398–1410. doi:10.1175/1520-0426(2001)018<1398:Stpolt>2.0.Co;2.

Ralston, D. K., Jiang, H. S., & Farrar, J. T. (2013). Waves in the Red Sea: Response to monsoonal and mountain gap winds. *Continental Shelf Research, 65*, 1–13. doi:10.1016/J.Csr.2013.05.017.

Skamarock, W., Klemp, J., Dudhia, J., Gill, D., Barker, D., Dudha, M., et al. (2008). A description of the advanced research WRF ver 30. Technical Note. NCAR/TN-475+STR. 113.

Sofianos, S. S., & Johns, W. E. (2001). Wind induced sea level variability in the Red Sea. *Geophysical Reseach Letters, 28*(16), 3175–3178. doi:10.1029/2000gl012442.

Sofianos, S. S., & Johns, W. E. (2002). An oceanic general circulation model (OGCM) investigation of the Red Sea circulation, 1. Exchange between the Red Sea and the Indian Ocean. *Journal of Geophysical Research*: *Oceans*, *107*(C11), doi:Artn 3196, doi:10.1029/2001jc001184.

Sofianos, S. S., Johns, W. E., & Murray, S. P. (2002). Heat and freshwater budgets in the Red Sea from direct observations at Bab el Mandeb. *Deep-Sea Research Part II, 49*(7–8), 1323–1340. doi:10.1016/S0967-0645(01)00164-3. (Pii S0967-0645(01)00164-3).

Stohl, A., Forster, C., Frank, A., Seibert, P., & Wotawa, G. (2005). Technical note: The Lagrangian particle dispersion model FLEXPART version 6.2. *Atmospheric Chemistry and Physics, 5*, 2461–2474.

Veneziani, M., Griffa, A., Garraffo, Z. D., & Chassignet, E. P. (2005). Lagrangian spin parameter and coherent structures from trajectories released in a high-resolution ocean model. *Journal of Marine Research, 63*(4), 753–788. doi:10.1357/0022240054663187.

Veneziani, M., Griffa, A., Reynolds, A. M., & Mariano, A. J. (2004). Oceanic turbulence and stochastic models from subsurface Lagrangian data for the northwest Atlantic Ocean. *Journal of Physical Oceanography, 34*(8), 1884–1906. doi:10.1175/1520-0485(2004)034<1884:Otasmf>2.0.Co;2.

Yao, F., Hoteit, I., Pratt, L. J., Bower, A. S., Köhl, A., Gopalakrishnan, G., & Rivas, D. (2014a). Seasonal overturning circulation in the Red Sea: 2. Winter circulation. *Journal of Geophysical Research: Oceans, 119*(4), 2263–2289. doi:10.1002/2013JC009331.

Yao, F., Hoteit, I., Pratt, L. J., Bower, A. S., Zhai, P., Köhl, A., & Gopalakrishnan, G. (2014b). Seasonal overturning circulation in the Red Sea: 1. Model validation and summer circulation. *Journal of Geophysical Research: Oceans, 119*(4), 2238–2262. doi:10.1002/2013JC009004.

Zhai, P., & Bower, A. (2013). The response of the Red Sea to a strong wind jet near the Tokar Gap in summer. *Journal of Geophysical Research: Oceans, 118*(1), 422–434. doi:10.1029/2012jc008444.

Zhan, P., Subramanian, A. C., Yao, F., & Hoteit, I. (2014). Eddies in the Red Sea: A statistical and dynamical study. *Journal of Geophysical Research*: *Oceans*, *119*(6), 3909–3925, doi:10.1002/2013JC009563.